Dalton Transactions

ROYAL SOCIETY OF CHEMISTRY

PAPER

View Article Online
View Journal | View Issue

Cite this: *Dalton Trans.*, 2023, **52**, 297

Solvothermal synthesis of nanoscale $BaTiO_3$ in benzyl alcohol–water mixtures and effects of manganese oxide coating to enhance the PTCR effect†

Min Zhang, [a] Thomas Caldwell, [a] Andrew L. Hector, *[a] Nuria Garcia-Araez [a,b] and Joseph Falvey [a]

Received 12th October 2022,
Accepted 6th December 2022

DOI: 10.1039/d2dt03307k

rsc.li/dalton

A solvothermal method using various benzyl alcohol/water solvent mixtures has been used to synthesise phase pure nanocrystalline $BaTiO_3$ samples with varying particle sizes in the range of 11–139 nm. The crystallite/particle size of $BaTiO_3$ shows an overall decrease as the benzyl alcohol percentage increases, especially at higher percentages (≥80%) of benzyl alcohol. The decrease in crystallite/particle size can be attributed to the increased viscosity of the solvent mixture when raising the percentage of benzyl alcohol. A manganese oxide coating applied to the $BaTiO_3$ surface had a negligible impact on its microstructure and morphology, but significantly enhanced the observed positive temperature coefficient of resistance. This research has been carried out to allow the development of smaller $BaTiO_3$ particles for use in new battery, capacitor and thermistor technologies, whilst maintaining the PTCR property of the material that is typically observed in larger particle sizes.

1. Introduction

Owing to its outstanding ferroelectric and dielectric properties, barium titanate ($BaTiO_3$) has been widely used in multilayer capacitors, thermistors, electro-optical and electromechanical devices, *etc*.[1] $BaTiO_3$ is a white crystalline solid that adopts the perovskite unit cell structure, following the classic ABO_3 arrangement at high temperatures. At room temperature, $BaTiO_3$ is in the tetragonal phase where the cubic structure is elongated along the [001] axis forming a distorted perovskite material.[2,3] When the temperature is changed it goes through several phase transitions. At 393 K it undergoes a ferroelectric to paraelectric transition from a tetragonal to a cubic structure.[4]

$BaTiO_3$ is an insulator at room temperature. When appropriately doped, $BaTiO_3$ can present semiconducting behaviour, with a dielectric constant that changes with temperature and phase; it also exhibits an anomalous sharp jump in resistivity at the Curie temperature and this property is known as a positive temperature coefficient of resistivity (PTCR).[5] The resistance can increase over several orders of magnitude practically converting the semiconducting resistor state into an insulator above the Curie temperature.[6] It is agreed that the temperature–resistivity relationship is related to a grain boundary effect because the anomaly has not been observed in a single crystal of $BaTiO_3$.[7] The most accepted model describing the PTCR effect is the Heywang–Jonker model.[7–9] Above the Curie temperature, Heywang's theory suggested that a two-dimensional electron trap along the grain boundaries results in acceptor states and a depletion layer. Acceptor states attract electrons from the bulk, resulting in an electron depletion layer and a grain boundary barrier is set up. Since grain boundary permittivity follows the Curie–Weiss law, permittivity decreases with increasing temperature. The size of the grain boundary barrier also increases with temperature and as a result, resistivity increases sharply due to the resistivity being exponentially dependant on the size of the grain boundary barrier. As the temperature is raised beyond the Curie temperature the energy of the trapped electrons increases. Once the energy of the trapped electrons matches the energy of the Fermi level, the electrons jump to the conduction band. As a result, the resistivity increases exponentially up to a maximum after which the increase in resistivity is halted.[7,8] Below the Curie temperature, Jonker's theory suggested that the polarisation of the crystal structure reduces the potential barrier height resulting in reduced grain boundary resistance.[7,9]

$BaTiO_3$ is of interest in the electronics industry due to its exciting electrical and physical properties. Particularly, for its

[a]*School of Chemistry, University of Southampton, Highfield, Southampton SO17 1BJ, UK. E-mail: A.L.Hector@soton.ac.uk*
[b]*The Faraday Institution, Quad One, Harwell Campus, Didcot OX11 0RA, UK*
† Electronic supplementary information (ESI) available. See DOI: https://doi.org/10.1039/d2dt03307k

usage in multilayer ceramic capacitors (MLCCs) where the dielectric constant of the material is of high importance; and for use in PTCR devices where the PTCR effect is applied to control resistance in a circuit at a certain temperature in the form of thermistors.[5,10] This PTCR effect has recently been used by ourselves to prevent thermal runaway in batteries.[11] MLCCs based upon formulations of $BaTiO_3$ have superior frequency characteristics, high reliability, high breakdown voltage and reduced costs associated with their synthesis. These key characteristics of $BaTiO_3$-based MLCCs allow $BaTiO_3$ compounds to compete with conventional high-capacitance Al or Ta electrolytic capacitors.[12] The miniaturisation of electronic devices means that $BaTiO_3$ needs to be created on a smaller and smaller scale to allow for thin ceramic layers to be used in multilayer capacitors that don't compromise the excellent dielectric properties of the larger particle sizes.

Synthesis of these superior nanoscale materials needs to be fast and efficient using low-temperature synthesis routes such as hydro/solvothermal methods.[13,14] Hydrothermal methods are known to produce extremely fine particles with a narrow size range and a spherical morphology.[15] Our previous study found that the reaction temperature and Ba/Ti precursor ratio/concentration affect the crystallite/particle size, morphology and composition of $BaTiO_3$ in hydrothermal synthesis.[16] Also, benzyl alcohol has been proved to be a versatile solvent for the synthesis of transition metal oxide nanoparticles with good control of crystallisation, particle size, morphology, *etc.*[17–22] Here, a solvothermal method using benzyl alcohol/water solvent mixtures is applied, with the aim of synthesising phase pure nanocrystalline $BaTiO_3$ samples with small crystallites. The effects of the solvent on the crystallite size, morphology and composition of $BaTiO_3$ are examined and linked to changes in viscosity and solubilities in the mixture. A manganese oxide coating is also applied on the surface of $BaTiO_3$ and found to enhance the PTCR effect exhibited by $BaTiO_3$.

2. Experimental

2.1. Materials synthesis

The $BaTiO_3$ samples were prepared *via* a solvothermal synthesis, as illustrated in Scheme 1. Varying percentages (0–100%) of benzyl alcohol ($C_6H_5CH_2OH$, ≥99% purity, ACROS Organics) and deionised water emulsions were made as solvents in solvothermal synthesis. The sample labels and corresponding benzyl alcohol percentages in solvents are specified in the results and discussion section. The Ti precursor was produced by adding $Ti(OCH(CH_3)_2)_4$ (0.89 g, ≥97% purity, Sigma Aldrich) slowly, dropwise with stirring to 15 mL of the ice-cold mixture of distilled water and benzyl alcohol. A white precipitate of TiO_2 formed. Stirring in an ice bath for a further 1 h resulted in a milky white suspension without clumps of particles. The mixture was stirred at room temperature for a further 2 h. As a Ba precursor, the Ba $(OH)_2{\cdot}8H_2O$ (1.97 g, ≥98% purity, Emsure) was dissolved/dispersed in 55 mL of the distilled water and benzyl alcohol mixture. The ratio of Ba and Ti precursors was kept at 2 : 1 for each synthesis. The Ti precursor suspension, once it had reached room temperature, was added dropwise to the Ba precursor solution/suspension, retaining the cloudy white colour. The reaction mixture was then sealed in a Teflon-lined autoclave and heated at 120 °C for 16 h. The resulting product settled to the bottom of the autoclave and appeared as a white powder. The clear benzyl alcohol and water solvent mixture was decanted off, and the white powder product was washed with diluted HCl solution once and deionised water three times, then dried in an oven at 80 °C for 12 h. The $BaTiO_3$ powder was ground using a pestle and mortar.

The solution used for manganese oxide coating was prepared by mixing $Mn(OOC_2H_3)_2{\cdot}4H_2O$ (≥99% purity, Sigma Aldrich) with C_2H_5OH (≥99.8% purity, Fisher Scientific). An appropriate amount of $BaTiO_3$ powder was dispersed in

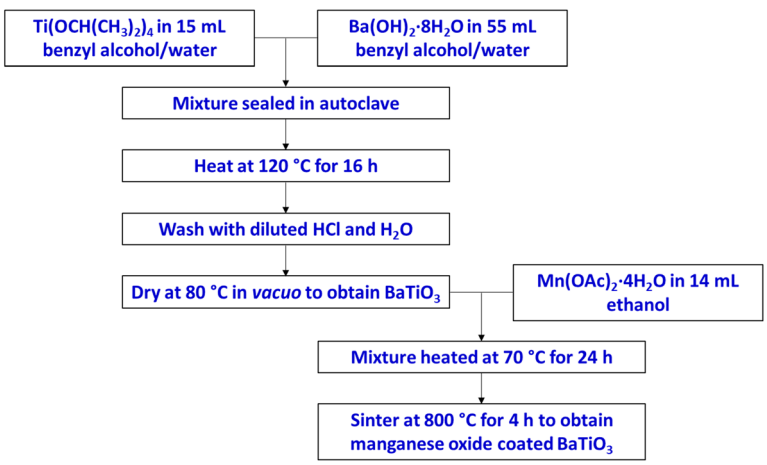

Scheme 1 Solvothermal synthesis to prepare $BaTiO_3$, using solvents with various percentages of benzyl alcohol and water; and the preparation procedure of manganese oxide coating onto $BaTiO_3$ samples.

the Mn-sol solution, so that the weight ratio of Mn $(OAc)_2{\cdot}4H_2O$ to $BaTiO_3$ powder was 5 : 95. These were dried at 70 °C for 24 h. The obtained powder was ground, pressed into a pellet and sintered at 800 °C for 4 h to obtain the manganese oxide coated $BaTiO_3$ sample, as illustrated in Scheme 1.

2.2. Materials characterisation

X-ray diffraction (XRD) was carried out using a Bruker D2 Phaser with Cu-K_α radiation. Rietveld fits to the XRD patterns were performed using the GSAS package.[23] The crystallite sizes were calculated from the Lorentzian crystallite size broadening coefficient refined in the Rietveld fits to the XRD patterns, according to $p = \frac{18000K\lambda}{\pi L_x}$, where p is the crystallite size (unit: nm), K is the Scherrer constant, λ is the wavelength of the incident X-rays (unit: nm), and L_x is the refined crystallite size broadening value.[23] In some of the Rietveld fits, the crystallite size broadening and the strain broadening are highly correlated, so a fixed strain broadening value from patterns with a low correlation has been applied to the rest of the Rietveld fits. Raman spectroscopy was carried out using a Renishaw inVia confocal microscope, and the spectra were analysed using the WiRE 4.1 software. Scanning electron microscopy (SEM) images were collected using a JEOL JSM-6500F operated at 10 kV, and images were analysed using the ImageJ software and Gaussian function. Transmission electron microscopy (TEM) micrographs were collected using an FEI Tecnai T12 (120 kV). Thermogravimetric analysis (TGA) used a Netzsch TG 209 F1 Libra with samples heated from 25 to 1000 °C under an Ar atmosphere. X-ray photoelectron spectroscopy (XPS) was collected with a Kratos Axis Supra spectrometer with a monochromated Al K_α X-ray source (1486.69 eV) at 15 mA emission and 12 kV HT (180 W) and a spot size/analysis area of 700 × 300 μm. High-resolution core peak spectra were recorded using a pass energy of 20 eV, step size of 0.1 eV and sweep time of 60 s. Survey spectra were obtained using a pass energy of 160 eV. Sample charging was prevented by using an electron flood gun with a filament current of 0.4 A, charge balance of 2 V and filament bias of 4.2 V. All data were recorded at a base pressure of below 9×10^{-9} Torr and a room temperature of 294 K. Spectra were analysed using Casa XPS software. Spectra were calibrated to the main line of the carbon 1s spectrum (adventitious carbon) set to 284.8 eV. Core peaks were analysed with a nonlinear Shirley-type background.[24] The peak positions and areas were optimized using a weighted least-squares fitting method with 70% Gaussian and 30% Lorentzian line shapes. Several spectral analyses were applied at different positions for each sample to ensure the results were statistically reliable. Electrochemical tests were carried out using a Biologic potentiostat. The absolute values of conductivities and PTCR effects were obtained from the current–voltage plots on uncoated and manganese oxide coated $BaTiO_3$ discs. Current–voltage measurements were performed at 20 mV s^{-1} in the range of −1 to +1 V at different temperatures.

3. Results and discussion

3.1. Effects of the solvent on the crystallite size, morphology and composition of $BaTiO_3$ in solvothermal synthesis

$BaTiO_3$ samples have been produced using benzyl alcohol/water solvent mixtures with various percentages of benzyl alcohol in solvothermal syntheses, to investigate the effects of the solvent on the crystallite size, morphology and composition of $BaTiO_3$. The sample labels and corresponding benzyl alcohol percentages (0–100%) in solvents are specified in Table 1.

Fig. 1a shows the XRD patterns of $BaTiO_3$ samples from solvothermal synthesis using benzyl alcohol/water solvent mixtures with various benzyl alcohol percentages. All the XRD peaks of the produced $BaTiO_3$ samples can be attributed to phase-pure $BaTiO_3$, since no impurity phases were detected. Habib *et al.* observed a $BaCO_3$ impurity in hydrothermal $BaTiO_3$ samples, which is formed through the reaction of Ba^{2+} ions in the solution and CO_2 in the air during the synthesis.[25] In our work, the impurities like $BaCO_3$ that may have formed in the solvothermal synthesis of $BaTiO_3$ have been removed by washing with diluted HCl, this can be confirmed by the absence of impurity peaks in the XRD patterns. Also, a finely divided amorphous TiO_2 with higher reactivity, freshly precipitated from the metal–organic $[Ti(OCH(CH_3)_2)_4]$ has been used as the Ti precursor in this work,[16] rather than crystalline rutile or anatase TiO_2 in the literature.[25,26] This increases the likelihood that it will fully react with the Ba precursor in solvothermal synthesis, thus avoiding any unreacted TiO_2 impurity to remain in the $BaTiO_3$ sample.[26]

As presented in Table 1, the crystallite sizes of $BaTiO_3$ samples are calculated from a size-strain analysis during the

Table 1 The variations of benzyl alcohol percentages (0–100%) in benzyl alcohol/water solvent mixtures in solvothermal syntheses of $BaTiO_3$ samples; crystallite sizes obtained from the Rietveld fits to the XRD patterns; particle sizes determined by using the ImageJ software and Gaussian function to analyse SEM and TEM images

Sample	Percentage of benzyl alcohol (%)	XRD crystallite size (nm)	SEM/TEM particle size (nm)
BTO-0	0	95.5 ± 1.1	109 ± 29
BTO-10	10	129 ± 2	116 ± 26
BTO-15	15	123 ± 2	137 ± 36
BTO-20	20	129 ± 2	134 ± 35
BTO-25	25	113 ± 2	117 ± 22
BTO-30	30	127 ± 2	135 ± 39
BTO-35	35	116 ± 2	135 ± 31
BTO-40	40	107 ± 2	126 ± 37
BTO-50	50	111 ± 2	125 ± 30
BTO-60	60	105.3 ± 1.4	115 ± 36
BTO-70	70	134 ± 2	139 ± 32
BTO-80	80	60.8 ± 0.5	68 ± 18
BTO-90	90	28.0 ± 0.2	39 ± 7
BTO-100	100	N/A	11 ± 4

Note that the yield of the BTO-100 sample is vanishingly small, thus no further investigation proceeded on this sample, except for the TEM characterisation.

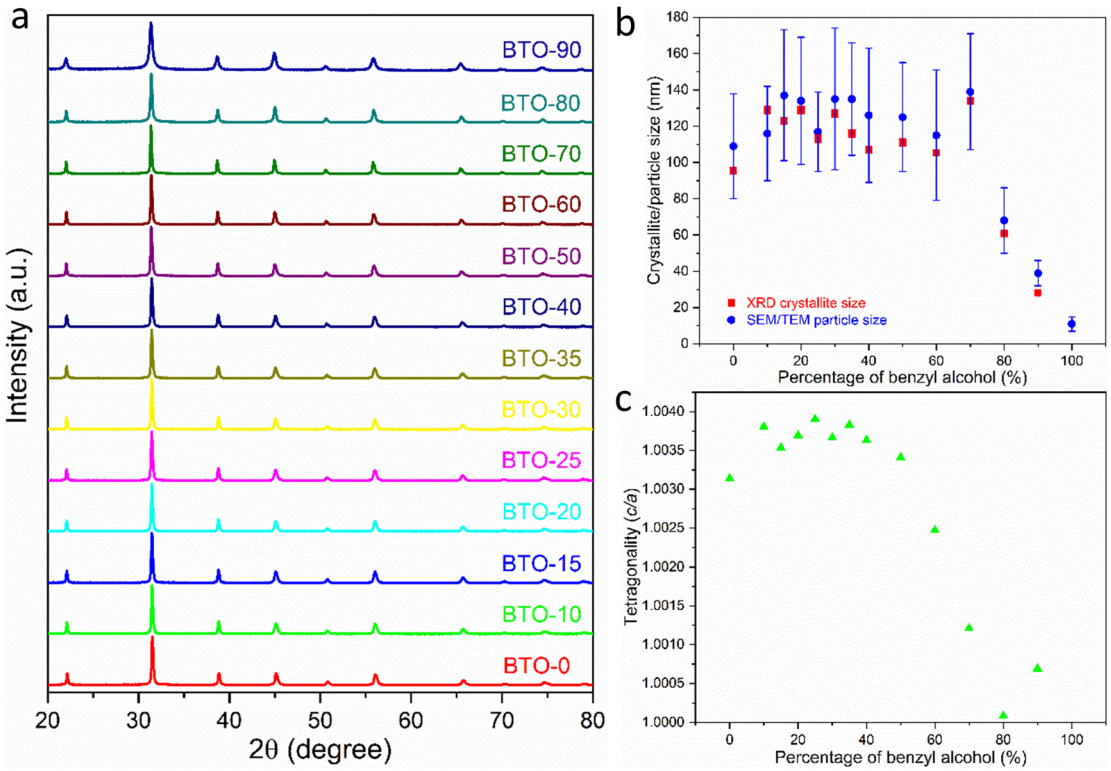

Fig. 1 (a) XRD patterns of $BaTiO_3$ samples synthesised *via* a solvothermal method with various benzyl alcohol/water solvent mixtures; (b) crystallite/particle size and (c) tetragonality (c/a) of $BaTiO_3$ samples plotted against benzyl alcohol percentage in solvothermal synthesis, the crystallite size and tetragonality obtained from the Rietveld fits to the XRD patterns, and the particle size determined by using the ImageJ software with a Gaussian function used to analyse SEM and TEM images (sample labels explained in Table 1).

Rietveld fits to the XRD patterns (Fig. S1†). The obtained lattice parameters (a and c), tetragonality (c/a), crystallite size broadening term (L_x) and reliability factors (R_{wp}, R_p) are listed in Table S1.† Fig. 1b shows the variation of the crystallite size of $BaTiO_3$ *versus* the benzyl alcohol percentage in solvothermal synthesis using benzyl alcohol/water solvent mixtures. The crystallite size of $BaTiO_3$ varies between 96 and 134 nm when the benzyl alcohol percentage is below 70%. By increasing the percentage of benzyl alcohol to higher than 80%, the crystallite size of $BaTiO_3$ drops to 28–61 nm. It shows an overall negative relationship between the benzyl alcohol percentage in solvothermal synthesis and the crystallite size of $BaTiO_3$. The trend, however, is non-linear with the negative relationship being more obvious towards higher percentages (≥80%) of benzyl alcohol. The decrease in crystallite size can be attributed to the increased viscosity of the solvent mixture when raising the percentage of benzyl alcohol, which can decrease the mass transport to growing crystallite surfaces, thus resulting in reduced $BaTiO_3$ crystallite size.

It has been reported that the $BaTiO_3$ with a large tetragonality is crucial in achieving the multilayer capacitor with a large capacitance,[27] and the tetragonality (c/a) can be used to indicate the degree of tetragonal-cubic distortion.[28] Fig. 1c shows the tetragonality variation of $BaTiO_3$ *versus* the benzyl alcohol percentage in solvothermal synthesis using benzyl alcohol/water solvent mixtures. The decreasing c/a value indicates that the tetragonality of $BaTiO_3$ decreases as the benzyl alcohol percentage is raised, especially at higher than 70%. Others have noted that the tetragonality of the crystal structure is generally decreased by the presence of defects in $BaTiO_3$.[29] The TGA analysis presented later suggests defect content may also be important here.

The tetragonality changes of the solvothermally prepared $BaTiO_3$ samples can also be probed by Raman spectroscopy. As presented in Fig. 2a, the Raman spectrum of the tetragonal $BaTiO_3$ exhibits the Raman active modes E(TO), A1(TO) at ~180 cm^{-1}, A1(TO) at ~270 cm^{-1}, E(LO + TO), B1 at ~307 cm^{-1}, E(TO), A1(TO) at ~515 cm^{-1} and E(LO), A1(LO) at ~720 cm^{-1}, while the cubic $BaTiO_3$ is Raman-inactive.[28] It has been reported that the sharp Raman peak at ~307 cm^{-1} (shaded in Fig. 2a) is extremely sensitive to the tetragonality of $BaTiO_3$, with its intensity rising when the crystal structure becomes more tetragonal.[30–32] Fig. 2b presents the variation of the relative integrated intensity of the Raman peak at 307 cm^{-1} for $BaTiO_3$ against the benzyl alcohol percentage in solvothermal synthesis using benzyl alcohol/water solvent mixtures. The decreasing integrated intensity of the Raman peak at 307 cm^{-1} indicates that the tetragonality of $BaTiO_3$ decreases as the benzyl alcohol percentage is raised, especially at higher than 70%. This trend is consistent with the results obtained from the XRD Rietveld analysis.

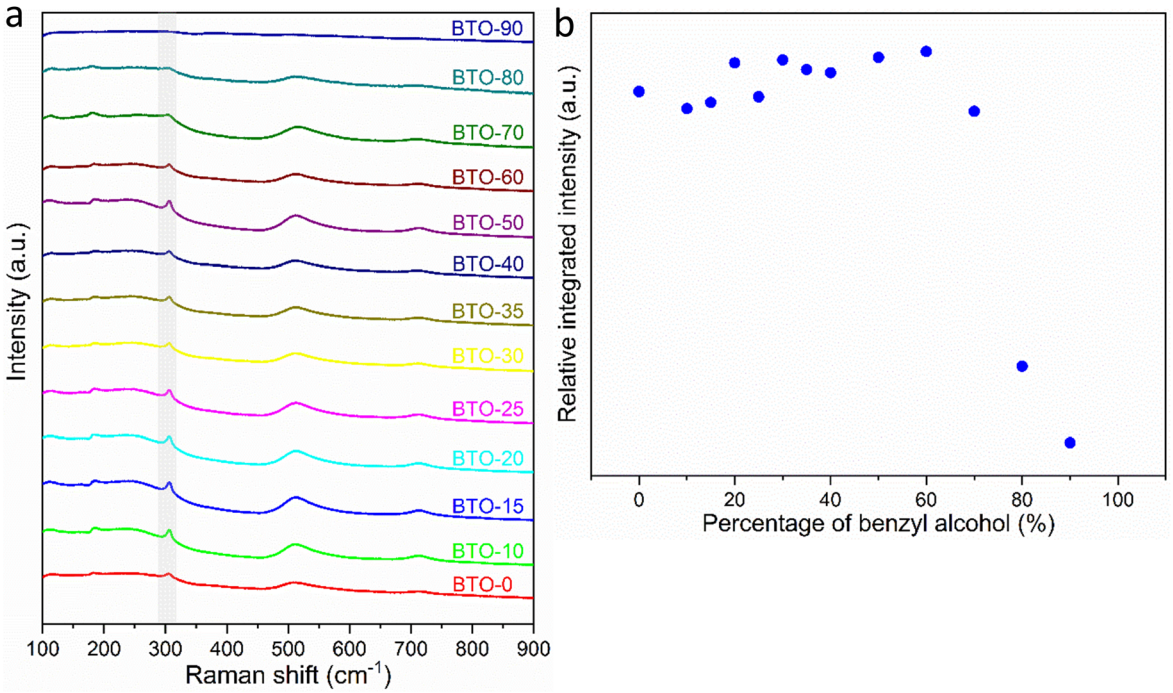

Fig. 2 (a) Raman spectra of $BaTiO_3$ samples synthesised *via* a solvothermal method with various benzyl alcohol percentages (0–90%) in benzyl alcohol/water solvent mixtures (peaks at ~307 cm^{-1} being marked as shaded); (b) relative integrated intensities of the Raman peak at 307 cm^{-1} for $BaTiO_3$ samples plotted against benzyl alcohol percentage in solvothermal synthesis (sample labels explained in Table 1).

To explore any trends between the particle size and morphology of $BaTiO_3$ and the benzyl alcohol percentage, Fig. 3 shows the SEM and TEM images and particle size distributions of $BaTiO_3$ samples synthesised with various benzyl alcohol/water solvent mixtures. By analysing the SEM and TEM images using the ImageJ software and Gaussian function, the particle sizes of $BaTiO_3$ samples have been determined and presented in Fig. 1b and Table 1. The $BaTiO_3$ samples synthesised using 0–70% benzyl alcohol exhibit relatively large particle sizes of 109–139 nm with well-defined morphologies. As the percentage of benzyl alcohol rises to higher than 80%, the particle size of $BaTiO_3$ drops to 39–68 nm, and the edge of particles becomes ill-defined. When 100% benzyl alcohol is used, the $BaTiO_3$ particle size decreases significantly to around 11 nm. This is similar to the phenomena observed in previous studies, which produced $BaTiO_3$ with particle sizes of ≤10 nm using 100% benzyl alcohol in solvothermal syntheses.[17,18,33,34] It can be concluded that the particle size of $BaTiO_3$ decreases as the benzyl alcohol percentage is raised, especially at higher than 80%. The decrease in particle size can be attributed to the increased viscosity of the solvent mixture when raising the percentage of benzyl alcohol, as discussed above. This trend agrees with the result obtained from the Rietveld fits to the XRD data.

TGA was performed for $BaTiO_3$ samples synthesised with benzyl alcohol percentages of 0, 20%, 40%, 60%, 80% and 90% in benzyl alcohol/water solvent mixtures. Fig. 4a and Table S2† show the mass losses of the $BaTiO_3$ powders in the TGA analyses when increasing the temperature from 25 to 1000 °C under the Ar atmosphere. The $BaTiO_3$ samples synthesised using 0% to 60% of benzyl alcohol exhibit total mass losses of 0.3% to 1.2%. The samples appear to have little or no water or benzyl alcohol adsorbed onto the surfaces as there are no mass losses below ~200 °C.[35] The large drops in masses occurred in the range of ~200–800 °C, which is within the range where it can be attributed to the loss of the surface hydroxyl and aryloxide groups in $BaTiO_3$.[36,37] The $BaTiO_3$ samples synthesised using 80% and 90% benzyl alcohol exhibit much larger mass losses of 5.0% and 7.6%, respectively, which started to occur right after heating. The mass losses occurring below ~200 °C are caused by the loss of surface water and benzyl alcohol groups that are physically adsorbed onto the particle surfaces.[35] The remaining mass losses occurred in the temperature range of ~200–800 °C, which are 3.7% and 5.8% for $BaTiO_3$ samples synthesised using 80% and 90% benzyl alcohol, respectively, can be attributed to the loss of surface hydroxyl and aryloxide defects in $BaTiO_3$.[37,38] The TGA characterisation suggests that as the benzyl alcohol percentage increases to higher than 80%, there is a greater amount of mass lost when the $BaTiO_3$ sample is heated.

All six $BaTiO_3$ samples show mass losses related to the losses of surface hydroxyl and aryloxide defects in $BaTiO_3$. However, only the $BaTiO_3$ samples synthesised using ≥80% benzyl alcohol exhibit the losses of adsorbed surface water and benzyl alcohol groups. This can be attributed to a smaller particle size having a greater surface area, thus more water and benzyl alcohol groups can be adsorbed onto the particle

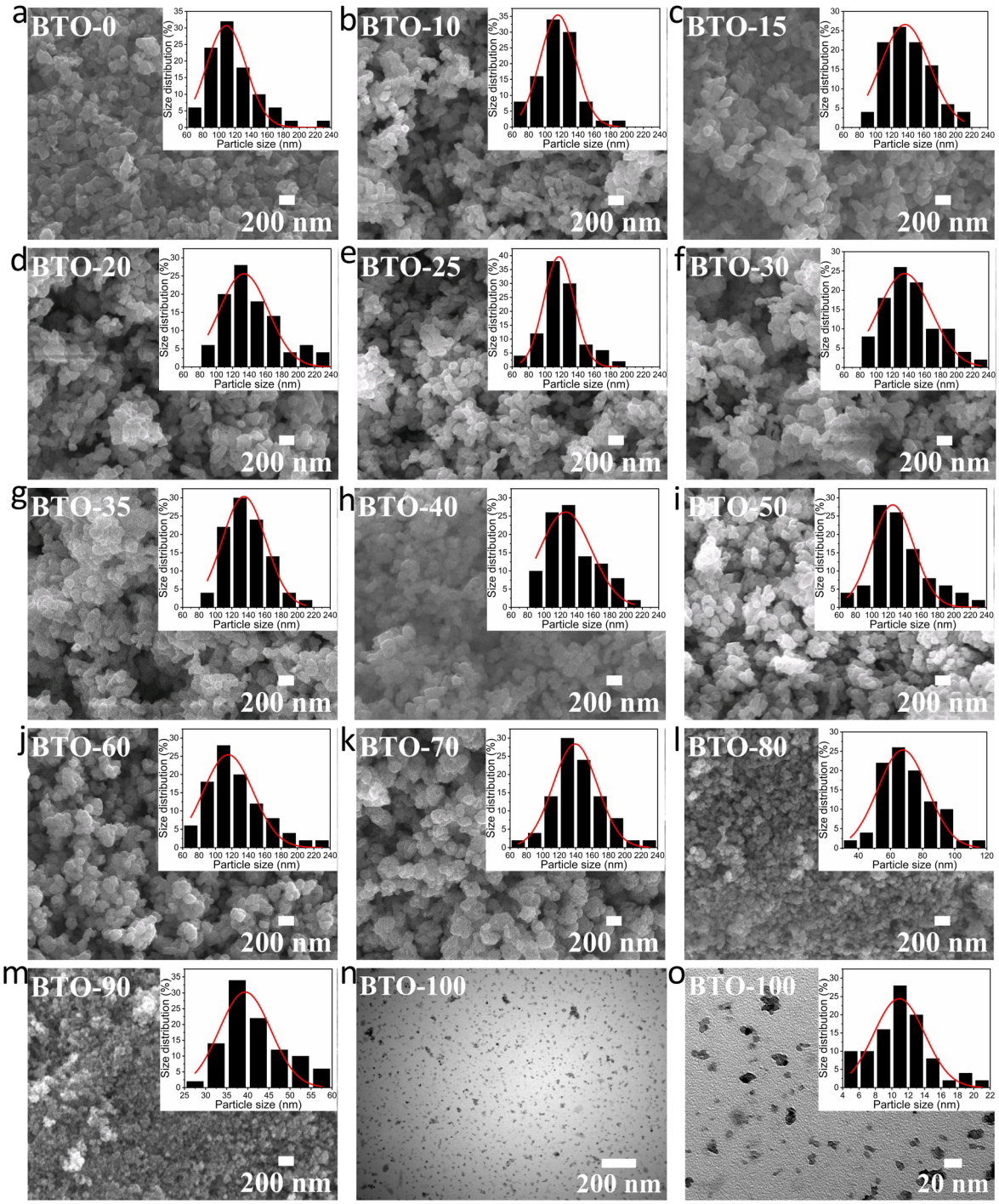

Fig. 3 (a–m) SEM images of $BaTiO_3$ samples synthesised *via* a solvothermal method with various benzyl alcohol percentages (0–90%) in benzyl alcohol/water solvent mixtures; (n) and (o) TEM images of $BaTiO_3$ sample synthesised using 100% benzyl alcohol (sample labels explained in Table 1); inserted patterns to show the particle sizes of the samples determined using the ImageJ software, and the size distributions analysed with a Gaussian function.

surface.[35] Also, the increasing amount of surface hydroxyl and aryloxide defects can be linked to the larger surface area of crystallites when formed using higher percentages of benzyl alcohol.[35,37] The $BaTiO_3$ samples prepared using 0% to 60% of benzyl alcohol exhibit particle sizes of 109 to 134 nm, and the samples synthesized with 80% and 90% of benzyl alcohol show much smaller particle sizes of 68 and 39 nm, respectively. Increasing the percentage of benzyl alcohol in solvothermal synthesis produces $BaTiO_3$ with a smaller particle size and a larger surface area, which results in more hydroxyl and

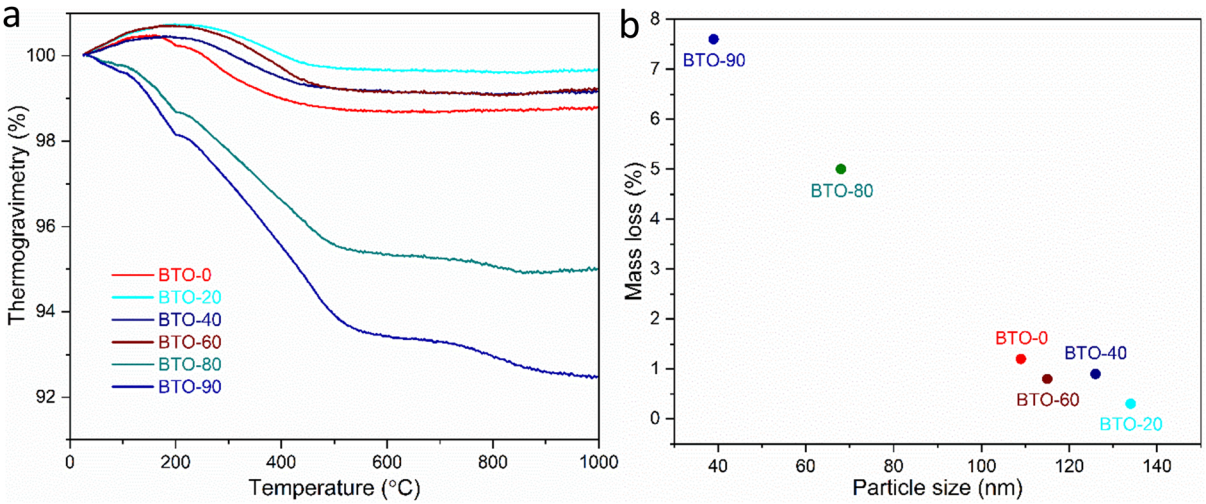

Fig. 4 (a) TGA curves and (b) mass losses plotted against particle sizes of $BaTiO_3$ samples synthesised *via* a solvothermal method with various benzyl alcohol percentages (0, 20%, 40%, 60%, 80% and 90%) in benzyl alcohol/water solvent mixtures, examined by heating from 25 to 1000 °C under Ar atmosphere (sample labels explained in Table 1).

aryloxide defects in the sample, and therefore a larger mass loss in the TGA analysis (Fig. 4b).

3.2. Microstructure, morphology and electrochemistry of $BaTiO_3$ modified with manganese oxide coating

The $BaTiO_3$ sample synthesised *via* a solvothermal method using 60% of benzyl alcohol in the benzyl alcohol/water solvent mixture (denoted as BTO-60) was selected for coating, as it has a relatively small particle size and low level of defects in the sample. Manganese oxide coating was prepared by mixing the Mn precursor ($Mn(OAc)_2{\cdot}4H_2O$) with $BaTiO_3$ powder in ethanol to deposit Mn ions on the surface of the $BaTiO_3$ powder, then firing at 800 °C for 4 h to obtain the manganese oxide coated $BaTiO_3$ sample (denoted as BTO-60-M).

The XRD patterns of uncoated and manganese oxide coated $BaTiO_3$ samples (Fig. 5a) can be attributed to tetragonal $BaTiO_3$ with perovskite structure, suggesting that the coating process does not affect the microstructure of $BaTiO_3$. The characteristic peaks of manganese oxide are not detectable in coated $BaTiO_3$ composite due to its low concentration. The crystallite sizes of uncoated and manganese oxide coated $BaTiO_3$ samples (Fig. 5c and Table 2) are 105 and 115 nm, respectively, calculated from the Lorentzian crystallite size broadening term in the Rietveld fits to the XRD patterns (Fig. 5b and Fig. S1†). The obtained lattice parameters (a and c), tetragonality (c/a), crystallite size broadening term (L_x) and reliability factors (R_{wp}, R_p) are listed in Table S3.†

The SEM images of uncoated and manganese oxide coated $BaTiO_3$ samples (Fig. 6a and b) show that the manganese oxide coating has a negligible impact on the morphology of $BaTiO_3$. The particle sizes of uncoated and manganese oxide coated $BaTiO_3$ samples are 115 and 120 nm, respectively (Fig. 6c and Table 2), determined by analysing SEM images

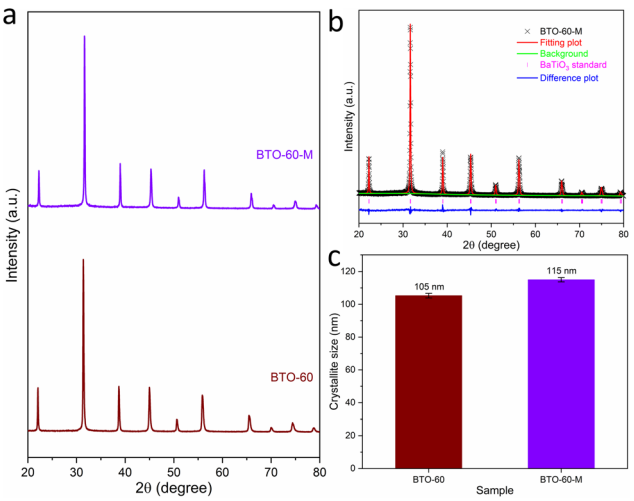

Fig. 5 (a) XRD patterns of BTO-60 and BTO-60-M samples; (b) Rietveld fit to the XRD pattern of BTO-60-M sample; (c) crystallite sizes obtained from the Rietveld fits to the XRD patterns of BTO-60 and BTO-60-M samples (sample labels explained in Table 2).

Table 2 The uncoated and manganese oxide coated $BaTiO_3$ samples synthesised using 60% of benzyl alcohol in benzyl alcohol/water solvent mixtures in solvothermal syntheses; crystallite sizes obtained from the Rietveld fits to the XRD patterns; particle sizes determined by using the ImageJ software and Gaussian function to analyse SEM images

Sample	Percentage of benzyl alcohol (%)	XRD crystallite size (nm)	SEM particle size (nm)
BTO-60	60	105.3 ± 1.4	115 ± 36
BTO-60-M	60	115.0 ± 1.3	120 ± 30

using the ImageJ software and Gaussian function. The particle size of manganese oxide coated $BaTiO_3$ is slightly larger than the uncoated $BaTiO_3$ sample, which is most likely due to a

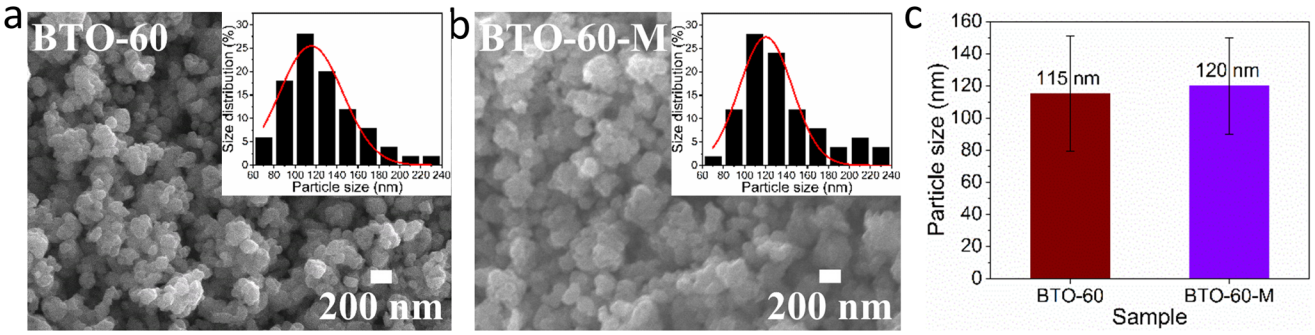

Fig. 6 (a) and (b) SEM images of BTO-60 and BTO-60-M samples; inserted patterns to show the particle sizes of the samples determined using the ImageJ software, and the size distributions analysed with a Gaussian function; (c) particle sizes of BTO-60 and BTO-60-M samples (sample labels explained in Table 2).

manganese oxide shell with a thickness of a few nanometres on the surface of the $BaTiO_3$ particles. This can be confirmed by the TEM images of the manganese oxide coated $BaTiO_3$ sample (Fig. 7b), which clearly shows a homogeneous coating layer on the surface of the $BaTiO_3$ particles, comparing to the uncoated $BaTiO_3$ sample (Fig. 7a).

To identify the composition of the manganese oxide coating, XPS has been applied on the uncoated and manganese oxide coated $BaTiO_3$ samples (Fig. 8). The survey spectra (Fig. S2†) confirm the presence of Ba, Ti and O for both samples, and the presence of Mn for manganese oxide coated sample. These two samples have similar Ba 3d and Ti 2p spectra (Fig. S2†). The Ba 3d spectrum splits into two spin states, with the binding energy of 778.3 and 793.5 eV for Ba $3d_{5/2}$ and Ba $3d_{3/2}$, respectively, and the spin–orbit splitting is 15.2 eV, indicating that the Ba exists in +2 oxidation state.[39] The Ti 2p peak splits into two spin states, *i.e.*, Ti $2p_{3/2}$ and Ti $2p_{1/2}$ at the binding energy of 457.9 and 463.8 eV, respectively, along with a satellite peak at 471.3 eV. The spin–orbit splitting for Ti $2p_{3/2}$ and Ti $2p_{1/2}$ is 5.9 eV, confirming the presence of the Ti^{4+} oxidation state in both samples.[40] Fig. 8 shows clear differences between the chemical environments present in the Mn 2p and O 1s spectra of these samples. For the manganese oxide coated $BaTiO_3$ sample, the Mn 2p spectrum splits into two spin states, *i.e.*, Mn $2p_{3/2}$ and Mn $2p_{1/2}$ at the binding energy of 641.1 and 652.9 eV, respectively, which is well in accordance with the values reported for manganese oxide.[41] The deconvolution of the Mn 2p core spectrum presented three characteristic peaks for each Mn $2p_{3/2}$ and Mn $2p_{1/2}$ associated with Mn^{2+}, Mn^{3+} and Mn^{4+} oxidation states (refers to MnO, Mn_2O_3 and MnO_2, respectively), with a clear dominance of Mn^{2+} state in the manganese oxide coated $BaTiO_3$ sample.[42] For the uncoated $BaTiO_3$ sample, the O 1s spectrum consists of two peaks at the binding energy of 529.2 and 530.5 eV, corresponding to the lattice oxygen in $BaTiO_3$ and the oxygen in the surface hydroxyl and aryloxide defects, respectively.[43] While in the O 1s spectrum of manganese oxide coated $BaTiO_3$ sample, an additional peak appears at the binding energy of 529.6 eV corresponding to the Mn–O–Mn environment of oxygen, confirming the presence of manganese oxide.[42]

The temperature dependence of resistivity (PTCR effect) for the uncoated and manganese oxide coated $BaTiO_3$ samples are presented in Fig. 9. The PTCR in $BaTiO_3$ is a grain boundary effect that can be explained by the Heywang–Jonker model.[44,45] At around room temperature, the manganese oxide coated $BaTiO_3$ sample (1.68×10^7 Ω cm) exhibits a much lower resistivity than uncoated $BaTiO_3$ (1.04×10^9 Ω cm). This has

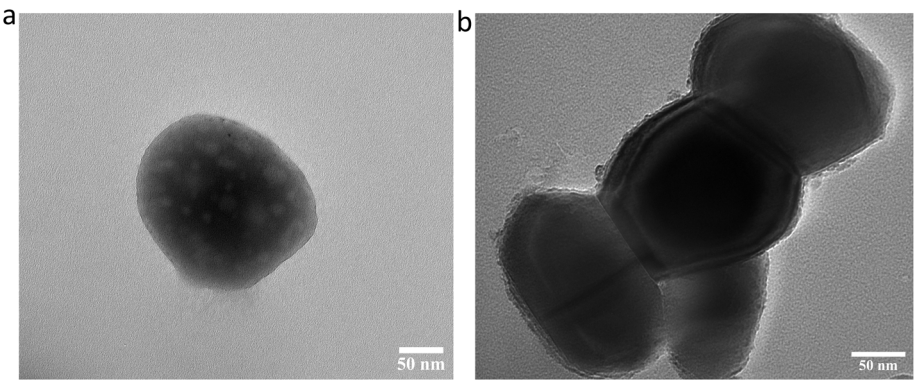

Fig. 7 TEM images of (a) BTO-60 and (b) BTO-60-M samples (sample labels explained in Table 2).

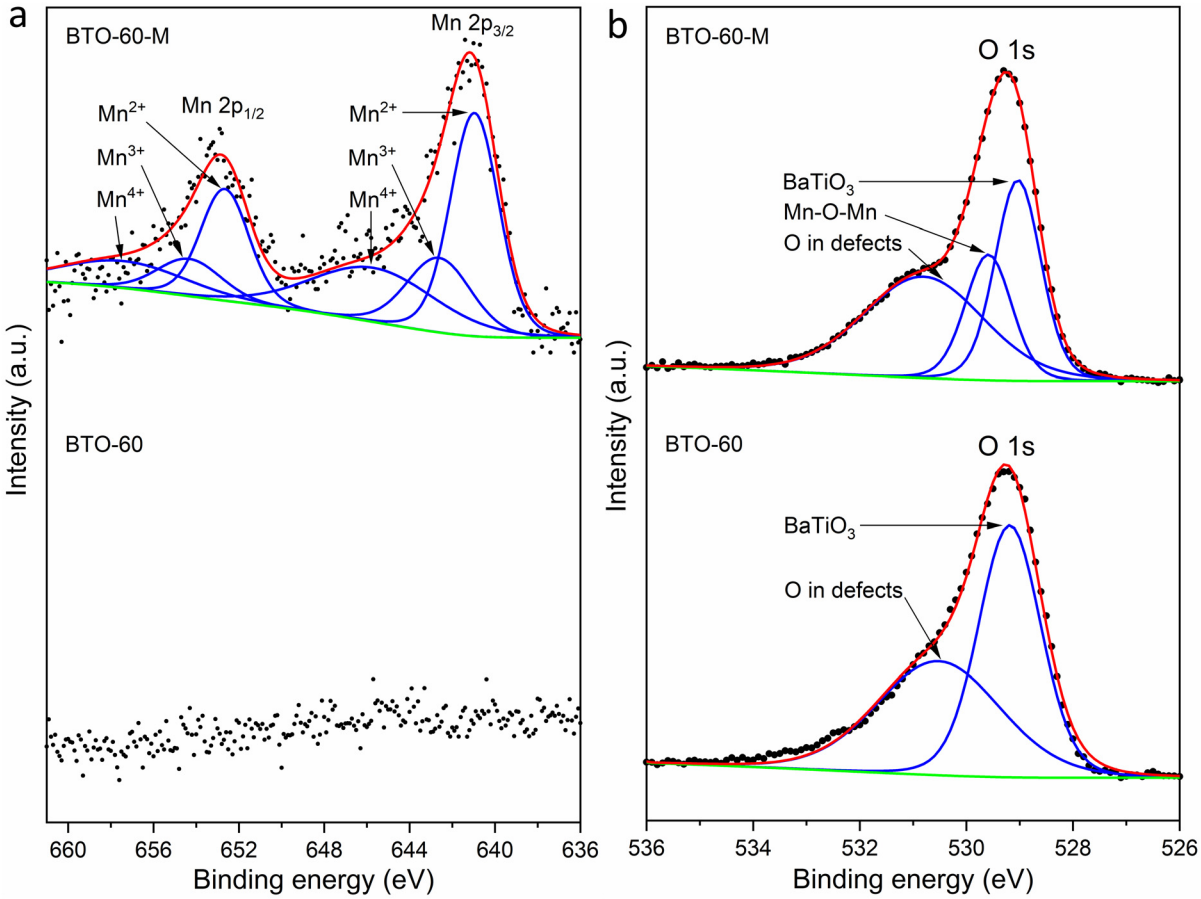

Fig. 8 (a) Mn 2p and (b) O 1s XPS spectra of BTO-60 and BTO-60-M samples (sample labels explained in Table 2). The data points and enveloped fitting plot are overlaid in black dots and a red line, respectively. The fitting peaks and background are shown in blue and green, respectively.

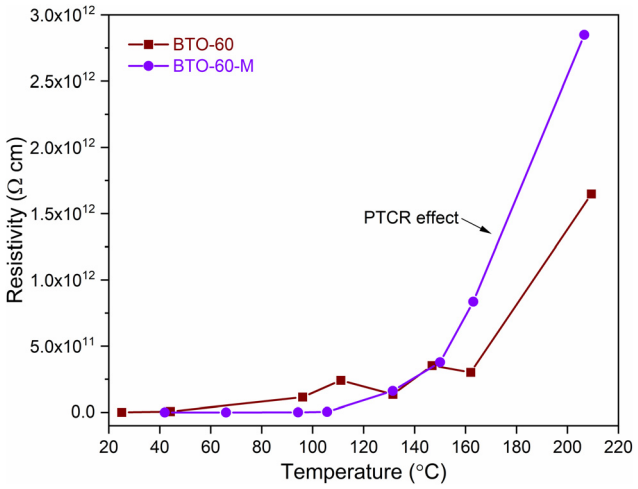

Fig. 9 Temperature dependence of resistivity (PTCR effect) for BTO-60 and BTO-60-M samples (sample labels explained in Table 2).

been attributed to the presence of the manganese oxide on the surface provides a relatively conducting network between the $BaTiO_3$ particles (Fig. 7b).[46–49] When the temperature increases to above the Curie temperature, according to the Heywang–Jonker model,[44,45] the potential barriers along the grain boundaries of both samples become fully effective,[45] thus the resistivities of both manganese oxide coated and uncoated $BaTiO_3$ samples increase to 2.85×10^{12} Ω cm and 1.65×10^{12} Ω cm, respectively. The manganese oxide coated $BaTiO_3$ sample shows a much larger resistivity jump (5.23 orders of magnitude) than the uncoated $BaTiO_3$ (3.20 orders of magnitude), which indicates that the manganese oxide coating enhances the PTCR effect of $BaTiO_3$. This is because some Mn ions substitute Ti^{4+} during coating, and preferentially segregate towards the grain boundary to form oxygen vacancies, barium vacancies and dopant manganese ions, resulting in a significant increase in the acceptor states concentration, which can act as electron traps at the grain boundary, leading to a rapid increase in resistivity above the Curie temperature.[50–52] The PTCR property in $BaTiO_3$ materials can be used to control the resistance in a circuit as a function of temperature in the form of thermistors, to be applied in the electronics industry including temperature sensing (temperature trips), overcurrent protection (self-resetting fuses) and electronic timing circuitry.[5,10] Also, this PTCR effect has recently been used by ourselves to prevent thermal runaway in batteries.[11]

4. Conclusion

Phase pure nanocrystalline $BaTiO_3$ samples with particle sizes ranging from 11 to 139 nm have been synthesised *via* a solvothermal method with various benzyl alcohol percentages in benzyl alcohol/water solvent mixtures. The crystallite/particle size of $BaTiO_3$ shows an overall decrease as the benzyl alcohol percentage increases, especially at higher percentages (≥80%) of benzyl alcohol. The decrease in crystallite/particle size can be attributed to the increased viscosity of the solvent mixture when raising the percentage of benzyl alcohol. The tetragonality of $BaTiO_3$ decreases as the benzyl alcohol percentage is raised, which can be ascribed to the presence of defects in $BaTiO_3$ synthesised using higher percentages of benzyl alcohol in solvothermal synthesis. The $BaTiO_3$ sample synthesised using 60% of benzyl alcohol exhibits both relatively small crystallite/particle size and fewer defects. A manganese oxide coating has been applied to this $BaTiO_3$ sample, which shows a negligible impact on its microstructure and morphology, whilst it can significantly enhance the PTCR effect of $BaTiO_3$.

Conflicts of interest

There are no conflicts to declare.

Acknowledgements

The authors thank EPSRC for support under the Industrial Strategy Challenge Fund (EP/R021295/1) and for an early career fellowship to NGA (EP/N024303/1). The XPS data collection was performed at the EPSRC National Facility for XPS ("HarwellXPS"), operated by Cardiff University and University College London, under Contract No. PR16195. Raw data used in preparation of the figures in the article and supplementary information are available at **https://doi.org/10.5258/SOTON/D2473**.

References

1 B. Jiang, J. Iocozzia, L. Zhao, H. Zhang, Y. W. Harn, Y. Chen and Z. Lin, *Chem. Soc. Rev.*, 2019, **48**, 1194–1228.
2 G. H. Kwei, A. C. Lawson and S. J. L. Billinge, *J. Phys. Chem.*, 1993, **97**, 2368–2377.
3 M. Acosta, N. Novak, V. Rojas, S. Patel, R. Vaish, J. Koruza, J. G. A. Rossetti and J. Rodel, *Appl. Phys. Rev.*, 2017, **4**, 041305.
4 M. A. Gomes, A. S. Lima, K. I. B. Eguiluz and G. R. Salazar-Banda, *J. Mater. Sci.*, 2016, **51**, 4709–4727.
5 P. Pinceloup, C. Courtois, A. Leriche and B. Thierry, *J. Am. Ceram. Soc.*, 1999, **82**, 3049–3056.
6 C. Teichmann and J. Töpfer, *J. Mater. Sci.: Mater. Electron.*, 2018, **29**, 17881–17886.
7 Y. L. Chen and S. F. Yang, *Adv. Appl. Ceram.*, 2013, **110**, 257–269.
8 W. Heywang, *Solid-State Electron.*, 1961, **3**, 51–58.
9 G. H. Jonker, *Solid-State Electron.*, 1964, **7**, 895–903.
10 M. Wegmann, R. Brönnimann, F. Clemens and T. Graule, *Sens. Actuators, A*, 2007, **135**, 394–404.
11 M. Zhang, S. Fop, D. Kramer, N. Garcia-Araez and A. L. Hector, *J. Mater. Chem. A*, 2022, **10**, 11587–11599.
12 C. Pithan, D. Hennings and R. Waser, *Int. J. Appl. Ceram. Technol.*, 2005, **2**, 1–14.
13 H.-W. Lee, S. Moon, C.-H. Choi and D. K. Kim, *J. Am. Chem. Soc.*, 2012, **95**, 2429–2434.
14 M. B. Park and N. H. Cho, *Appl. Surf. Sci.*, 2005, **244**, 418–421.
15 I. J. Clark, T. Takeuchi, N. Ohtori and D. C. Sinclair, *J. Mater. Chem.*, 1999, **9**, 83–91.
16 M. Zhang, J. Falvey, A. L. Hector and N. Garcia-Araez, *RSC Adv.*, 2022, **12**, 27809–27819.
17 M. Niederberger, G. Garnweitner, N. Pinna and M. Antonietti, *J. Am. Chem. Soc.*, 2004, **126**, 9120–9126.
18 M. Niederberger, N. Pinna, J. Polleux and M. Antonietti, *Angew. Chem.*, 2004, **116**, 2320–2323.
19 M. Niederberger, M. H. Bartl and G. D. Stucky, *J. Am. Chem. Soc.*, 2002, **124**, 13642–13643.
20 M. Niederberger, M. H. Bartl and G. D. Stucky, *Chem. Mater.*, 2002, **14**, 4364–4370.
21 M. Niederberger, G. Garnweitner, F. Krumeich, R. Nesper, H. Cölfen and M. Antonietti, *Chem. Mater.*, 2004, **16**, 1202–1208.
22 J. Polleux, N. Pinna, M. Antonietti and M. Niederberger, *Adv. Mater.*, 2004, **16**, 436–439.
23 A. Larson, R. Von Dreele, L. Finger, M. Kroeker and B. Toby, *J. Appl. Crystallogr.*, 2001, **34**, 210–213.
24 D. A. Shirley, *Phys. Rev. B: Solid State*, 1972, **5**, 4709–4714.
25 A. Habib, R. Haubner and N. Stelzer, *Mater. Sci. Eng., B*, 2008, **152**, 60–65.
26 H.-J. Chen and Y.-W. Chen, *Ind. Eng. Chem. Res.*, 2003, **42**, 473–483.
27 J.-M. Han, M.-R. Joung, J.-S. Kim, Y.-S. Lee, S. Nahm, Y.-K. Choi, J.-H. Paik and E. Suvaci, *J. Am. Ceram. Soc.*, 2014, **97**, 346–349.
28 M. B. Smith, K. Page, T. Siegrist, P. L. Redmond, E. C. Walter, R. Seshadri, L. E. Brus and M. L. Steigerwald, *J. Am. Chem. Soc.*, 2008, **130**, 6955–6963.
29 S. Wada, T. Suzuki and T. Noma, *J. Ceram. Soc. Jpn.*, 1995, **103**, 1220–1227.
30 M. El Marssi, F. Le Marrec, I. A. Lukyanchuk and M. G. Karkut, *J. Appl. Phys.*, 2003, **94**, 3307–3312.
31 Y. Shiratori, C. Pithan, J. Dornseiffer and R. Waser, *J. Raman Spectrosc.*, 2007, **38**, 1300–1306.
32 A. Mansuri, I. N. Bhatti, I. N. Bhatti and A. Mishra, *J. Adv. Dielectr.*, 2018, **8**, 1850024.
33 T. M. Stawski, S. A. Veldhuis, O. F. Göbel, J. E. Ten Elshof and D. H. A. Blank, *J. Am. Ceram. Soc.*, 2010, **93**, 3443–3448.
34 S. A. Veldhuis, W. J. Vijselaar, T. M. Stawski and J. E. ten Elshof, *Inorg. Chem.*, 2014, **53**, 13188–13196.
35 E. Ciftci, M. N. Rahaman and M. Shumsky, *J. Mater. Sci.*, 2001, **36**, 4875–4882.

36 E.-W. Shi, C.-T. Xia, W.-Z. Zhong, B.-G. Wang and C.-D. Feng, *J. Am. Ceram. Soc.*, 1997, **80**, 1567–1572.
37 P. Yu, B. Cui and Q. Shi, *Mater. Sci. Eng., A*, 2008, **473**, 34–41.
38 W. Cai, T. Rao, A. Wang, J. Hu, J. Wang, J. Zhong and W. Xiang, *Ceram. Int.*, 2015, **41**, 4514–4522.
39 M. Arshad, W. Khan, P. Rajput, M. Kumar, M. Abushad and S. Husain, *Ceram. Int.*, 2022, **48**, 14156–14165.
40 D. Ehre, H. Cohen, V. Lyahovitskaya and I. Lubomirsky, *Phys. Rev. B: Condens. Matter Mater. Phys.*, 2008, **77**, 184106.
41 T. M. Alfareed, Y. Slimani, M. A. Almessiere, S. E. Shirsath, M. Hassan, M. Nawaz, F. A. Khan, E. A. Al-Suhaimi and A. Baykal, *Ceram. Int.*, 2022, **48**, 14640–14651.
42 L. Liu, J. Liu and M. Guo, *J. Environ. Chem. Eng.*, 2022, **10**, 107448.
43 I. C. Amaechi, G. Kolhatkar, A. H. Youssef, D. Rawach, S. Sun and A. Ruediger, *RSC Adv.*, 2019, **9**, 20806–20817.
44 W. Heywang, *J. Am. Ceram. Soc.*, 1964, **47**, 484–490.
45 G. H. Jonker, *Solid-State Electron.*, 1964, **7**, 895–903.
46 P. H. Klose, *J. Electrochem. Soc.*, 1970, **117**, 854–858.
47 F. Hong, B. Yue, N. Hirao, Z. Liu and B. Chen, *Sci. Rep.*, 2017, **7**, 44078.
48 N. P. Arias, M. E. Becerra and O. Giraldo, *Nanomaterials*, 2019, **9**, 1156.
49 R. N. D. Guzman, A. Awaluddin, Y.-F. Shen, Z. R. Tian, S. L. Suib, S. Ching and C.-L. O'Young, *Chem. Mater.*, 1995, **7**, 1286–1292.
50 J. Qi, Z. Gui, Y. Wu and L. Li, *Mater. Chem. Phys.*, 2002, **73**, 97–100.
51 J. M. Prohinig, P. Kuegler, K. Reichmann, H. Hutter and S. Bigl, *J. Eur. Ceram. Soc.*, 2022, **42**, 2827–2835.
52 H. Donnerberg and A. Birkholz, *J. Phys.: Condens. Matter*, 2000, **12**, 8239–8247.